

# Mixed Metal-Organic Frameworks as Efficient Semi-Solid Electrolytes for Magnesium-Ion Batteries

Hagar K. Hassan,<sup>\*[a, b, c, d]</sup> Attila Farkas,<sup>[c]</sup> Alberto Varzi,<sup>[a, b]</sup> and Timo Jacob<sup>\*[a, b, c]</sup>

One of the main issues of metal organic framework (MOF)-based solid electrolytes (SE) is their high guest solvent content reaching up to >50 wt% of the total mass of SE pellets. The presence of large solvent amounts reduces the SE hardness and the electrochemical stability in presence of a magnesium (Mg) anode. Moreover, this often leads to misleading ionic conductivity values. In the present work, a strategy to minimize the guest solvent in MOF-based SE from 44–55 wt% to 20–30 wt% of the total SE's mass is presented. Moreover, mixed metal organic frameworks of different structures and crystallinity are demonstrated for the first time to enhance the ionic con-

ductivity of Mg<sup>2+</sup> ions inside the MOFs' structures. The presence of both highly crystalline and amorphous MOFs increases the degree of disorder in the mixture and consequently opens up extra pathways for Mg<sup>2+</sup> ion diffusion. The ionic conductivity of mixed MOFs [amorphous Mgpb3dc and crystalline  $\alpha$ -Mg<sub>3</sub>(HCOO)<sub>6</sub>] showed an enhanced value of  $3.8 \times 10^{-5}$  S cm<sup>-1</sup> at 30°C compared to  $1.1 \times 10^{-6}$  S cm<sup>-1</sup> for  $\alpha$ -Mg<sub>3</sub>(HCOO)<sub>6</sub>. Mixed MOF-SEs with a transference number ( $t_+$ ) of 0.335 showed a good stability in the presence of Mg electrodes with an enhanced reversibility upon galvanostatic cycling.

## Introduction

Metal-organic frameworks (MOFs) have attracted considerable attention in various fields of research and many applications due to their high surface area, high porosity, and good mechanical properties.<sup>[1–4]</sup> Therefore, this class of materials undergoes an ever-growing development for diverse potential applications.<sup>[5]</sup> The vast number of organic ligands and metal ion combinations offers the possibility of designing many different MOF structures, enabling a systematic tuning of their physicochemical properties.<sup>[6]</sup> By appropriately selecting metallic nodes and organic linkers, MOFs with various structures and functionalities have been successfully synthesized.<sup>[7,8]</sup> So far, MOFs have been generally synthesized under hydrothermal, mechanochemical, solvothermal, sonochemical, or even electrochemical conditions.<sup>[9]</sup> The solvothermal method is the most

commonly used to synthesize MOFs as it is simple and requires very little specialized equipment compared to the other methods, while the obtained materials maintain a high degree of porosity, crystallinity, and high surface area.<sup>[10]</sup> However, the reaction conditions such as temperature, cooling rate, reactants composition, and mixing solvents have a tremendous impact on structure, morphology, and size of the resulting products.<sup>[10–12]</sup> Therefore, it is crucial to synthesize MOFs under well-controlled conditions and systematically study the effects of different hydrothermal conditions on the structure and physicochemical properties of the resulting MOFs.

MOFs have afforded a great impact in the area of chemicals and gas storage due to their high porosity and surface area.<sup>[13–15]</sup> During the last few years, MOFs paved their way toward electrochemical energy storage applications such as supercapacitors<sup>[16,17]</sup> and batteries.<sup>[18–21]</sup> Additionally, MOFs have been used as precursors to synthesize various composites such as carbon and metal oxides/hydroxides, that can be used as active electrode materials for lithium-ion batteries.<sup>[22]</sup> Due to their electronically insulating behavior and high porosity, MOFs also showed great impact in the area of solid-state batteries as solid electrolyte matrices.<sup>[2,3,23–27]</sup> Long and co-workers<sup>[27]</sup> firstly reported high lithium-ion conductivities reaching  $0.31$  mS cm<sup>-1</sup> from Li salts incorporated in Mg<sub>2</sub>(dobdc) (dobdc = 1,4-dioxido-2,5-benzenedicarboxylate) MOFs. The anions in lithium (Li) salts are bound to unsaturated Mg<sup>2+</sup> cation clusters leaving lithium ions free to migrate through the Mg<sub>2</sub>(dobdc) framework, finally resulting in high ionic conductivity values. Dincă et al.<sup>[24]</sup> reported ionic conductivities of  $1.3 \times 10^{-5}$ ,  $1.8 \times 10^{-5}$ , and  $8.8 \times 10^{-7}$  S cm<sup>-1</sup> for Li, Na, and Mg ions, respectively, when MIT-20 (a Cu<sup>2+</sup>-containing MOF) was used as matrix for solvated LiCl, NaSCN or MgBr<sub>2</sub> salts. Kitagawa and co-workers<sup>[26]</sup> studied the ionic conductivity of ZIF-8 (a Zr-based MOF) including a lithium-containing ionic liquid (Li-IL), whose conductivity reached  $0.1$  mS cm<sup>-1</sup> at room temperature. Beyond Li-ions,

[a] Dr. H. K. Hassan, Dr. A. Varzi, Prof. Dr. T. Jacob  
Helmholtz Institute of Ulm (HIU)

Helmholtz Str. 11, 89081 Ulm, Germany

[b] Dr. H. K. Hassan, Dr. A. Varzi, Prof. Dr. T. Jacob  
Karlsruhe Institute of Technology (KIT)

76021, Karlsruhe, Germany

E-mail: hagar.ibrahim@kit.edu

[c] Dr. H. K. Hassan, Dr. A. Farkas, Prof. Dr. T. Jacob

Institute of Electrochemistry

Ulm University

Albert-Einstein-Allee 47, 89081 Ulm, Germany

E-mail: Timo.jacob@uni-ulm.de

[d] Dr. H. K. Hassan

Faculty of Science

Cairo University

12613, Cairo, Egypt

Supporting information for this article is available on the WWW under <https://doi.org/10.1002/batt.202200260>

© 2022 The Authors. *Batteries & Supercaps* published by Wiley-VCH GmbH. This is an open access article under the terms of the Creative Commons Attribution Non-Commercial License, which permits use, distribution and reproduction in any medium, provided the original work is properly cited and is not used for commercial purposes.

MOFs have also shown promising results for Mg ion conduction. The group of Long et al.<sup>[1]</sup> studied the possibility of achieving high  $Mg^{2+}$  ion conductivities from  $Mg_2(dobdc)$ , comparable to the values obtained for  $Li^+$  ions. They investigated the ionic conductivities of different magnesium phenolates and  $Mg(TFSI)_2$  solvated by triglymes and incorporated in  $Mg_2(dobdc)$  as well as its expanded analogue  $Mg_2(dobpdc)$  ( $dobpdc$ : 4,4'-dioxidobiphenyl-3,3'-dicarboxylate). Based on their work, the expanded  $Mg_2(dobpdc)$  structure has the ability to incorporate a higher amount of Mg salts into its pores, thus allowing for higher ionic conductivities. Room temperature ionic conductivities of  $0.25\text{ mScm}^{-1}$  with  $Mg_2(dobpdc)$  and  $0.1\text{ mScm}^{-1}$  with  $Mg_2(dobdc)$  were reported.<sup>[1]</sup> However, the presence of 45–55 wt% solvent (related to the total mass of SEs) could be the reason for such high ionic conductivities which are rather close to what was reported for  $Li^+$  ions in another work from the same group.<sup>[27]</sup> This raises the question whether these high ionic conductivities are resulting from the free migration of  $Mg^{2+}$  ions inside the framework or whether the origin is in the high solvent extent. Additionally, there are no reported electrochemical tests proving the stability of such MOF-based SEs towards Mg electrodes. However, among the other reported  $Mg^{2+}$  ion conductors, MOF-based SEs are the only class of solid materials that showed reasonable room temperature ionic conductivities for  $Mg^{2+}$  with a minimum electronic contribution. The earliest examples of solid-state Mg ions conductors suffer from either very low ionic conductivity at room temperatures or high electronic conductivity. For example, magnesium zirconium phosphates showed an ionic conductivity of only  $2.9 \times 10^{-5}\text{ Scm}^{-1}$  at  $400^\circ\text{C}$ ,<sup>[28]</sup> while borohydride-based SEs such as  $Mg(BH_4)(NH_2)$  showed an ionic conductivity not exceeding  $10^{-6}\text{ Scm}^{-1}$  at  $150^\circ\text{C}$ .<sup>[29]</sup> Ethylenediamine derivatives of magnesium borohydride could deliver a higher ionic conductivity of  $6 \times 10^{-5}\text{ Scm}^{-1}$  at  $70^\circ\text{C}$ , and  $5 \times 10^{-8}\text{ Scm}^{-1}$  at room temperature.<sup>[30]</sup> On the other hand, Canepa et al. reported a  $Mg^{2+}$  ion mobility in ternary spinel chalcogenides with the general formula  $MgX_2Z_4$ , where  $X=(In, Y, Sc)$  and  $Z=(S, Se)$ .<sup>[31]</sup> Among all reported chalcogenides,  $MgSc_2Se_4$  showed an ionic conductivity of  $0.1\text{ mScm}^{-1}$  at room temperature.<sup>[31]</sup> However, this material has high electronic conductivity (0.04% of ionic conductivity) that hinders their use as battery electrolyte.<sup>[31]</sup> Fichtner et al.<sup>[32]</sup> reported two possible approaches to reduce the electronic conductivity of  $MgSc_2Se_4$  through the synthesis of Se-rich phases, and by doping  $Sc^{3+}$  with  $Ti^{4+}$  and  $Ce^{4+}$ . Unfortunately, these led to a reduction in the electronic conductivity to only 0.03% of the ionic conductivity which still seemed insufficient.

Herein, we propose a strategy to enhance the ionic conductivity of MOFs-based SEs through the simultaneous synthesis of a mixture of Mg-based MOFs. By controlling the hydrothermal reaction conditions between magnesium salt and 2,2'-bipyridine-3,3'-dicarboxylic acid ( $bp3dc$ ) in a DMF solvent, a mixture of MOFs,  $Mgbp3dc$  and  $\alpha\text{-Mg}_3(\text{HCOO})_6$ , further named MOF1, has been synthesized simultaneously. Upon thermal activation  $Mgbp3dc$  undergoes amorphization, leaving the crystallinity of  $\alpha\text{-Mg}_3(\text{HCOO})_6$  unaffected, finally leading to a

mixture of  $\alpha\text{-Mgbp3dc}$  and  $\alpha\text{-Mg}_3(\text{HCOO})_6$ . A strategy to reduce the solvent extent in MOFs-based solid electrolytes, while keeping a satisfactory ionic conductivity at room temperature is also presented. The activated MOF1 (a-MOF1)-based SEs with the lowest solvent content (20–30%) are investigated as promising  $Mg^{2+}$  ion conductors with an ionic conductivity of  $3.8 \times 10^{-5}\text{ Scm}^{-1}$  at  $30^\circ\text{C}$ .

## Results and Discussion

### Single-phase $[\text{Mg}(\text{bp3dc})(\text{H}_2\text{O})_4]_n$ coordination polymer

In this work,  $Mg^{2+}$  ions are used as metal nodes and  $bp3dc$  as organic linkers. Single crystals of  $[\text{Mg}(\text{bp3dc})(\text{H}_2\text{O})_4]_n$  (c- $Mgbp3d$ ) were obtained by the hydrothermal reaction of 0.5 mmol of  $Mg(\text{NO}_3)_2 \cdot 6\text{H}_2\text{O}$  with 0.5 mmol  $bp3dc$  ligand in 10 mL DMF at  $100^\circ\text{C}$  for three days before the slow solvent evaporation for few weeks. The phase quality was investigated by powder XRD (Figure 1a) and showed perfect agreement with the simulated XRD pattern obtained from CIF file CCDC-882772 reported by Zhang et al.<sup>[33]</sup> Looking into the structure of  $Mgbp3dc$  depicted in Figure 1(b and c), one can see that each  $bpda^{2-}$  molecule coordinates two  $Mg^{2+}$  ions and likewise each  $Mg^{2+}$  ion interacts with two  $bpda^{2-}$  ligands to generate a two-fold helical chain along the  $b$  direction. H-bonding interactions between the coordinated water molecules and the pyridyl N atoms, O—H···N, are responsible for 2D networks in the  $bc$  plane. While H-bonding interactions between the uncoordinated carboxylate oxygen atoms and the coordinated water molecules yield the 3D framework. Therefore, both O—H···O and O—H···N are responsible for binding the chains together. TGA analysis of  $Mgbp3dc$  ( $\text{H}_2\text{O})_4$  (Figure 1d) shows a mass loss up to  $100^\circ\text{C}$  due to removal of solvation molecules, then subsequent mass losses start from  $113^\circ\text{C}$  at which coordinated water molecules start to leave the crystals, being completely removed upon further heating to  $200^\circ\text{C}$  while the complex framework remains stable up to  $334^\circ\text{C}$ . As the hydrogen bonds are the reasons for 3D networking in  $Mgbp3dc$ , removal of water molecules may lead to amorphization and structure collapsing, a process that may hinder guest solvent removal from MOF. As shown from powder XRD (Figure 1a),  $Mgbp3dc$  undergoes an amorphization process and the structure loses its crystallinity upon thermal evacuation. It is worth mentioning that the crystallization of  $Mgbp3dc$  is very slow and requires at least a few weeks under the previously mentioned hydrothermal reaction conditions. It is found that by raising the synthesis temperature to  $120^\circ\text{C}$ , a highly crystalline powder of  $Mgbp3dc$  was rapidly precipitated after a hydrothermal reaction for 3 days as shown in Supporting Information Figure S1. The synthesis conditions of coordination polymers have a potential impact on the structure, quality, and morphology of the final product.<sup>[10]</sup> Therefore, the effect of changing the hydrothermal reaction conditions on the resulting product was investigated in a systematic way.

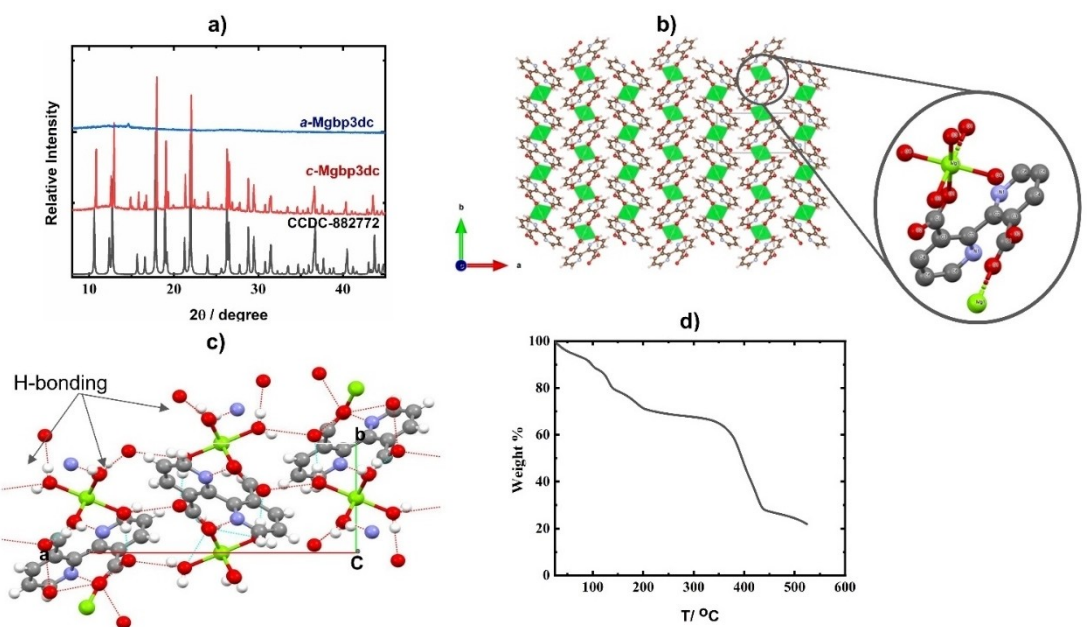


**Figure 1.** a) XRD of single phase Mgbp3dc and its amorphous structure,  $\alpha$ -Mgbp3dc, b) crystal structure of Mgbp3dc (Inset: its unit cell showing the coordination of Mg ion with two bp3dc and  $\text{H}_2\text{O}$  ligands), c) H-bonding in Mgbp3dc, and d) TGA of the powder form of Mgbp3dc synthesized at 120 °C.

### Effect of hydrothermal synthesis conditions

Increasing the metal to ligand ratio (M:L), changing the reaction period and the cooling rate are possible ways to enhance the reaction yields and to obtain high-quality crystals.<sup>[10,34]</sup> Therefore, various synthesis parameters have been tuned and the resulting structures have been investigated by powder XRD in order to obtain more insights into the hydrothermal reaction between Mg salt and bp3dc ligand.

The effect of the metal to ligand (M:L) ratio has been studied by the hydrothermal reaction at 120 °C for M:L ratios of 1:1, 2:1, and 3:1. All the reactions were carried out for 72 h followed by a slow-cooling to room temperature for another 72 h in a total reaction time of 6 days. Figure 2(a) shows the effect of the M:L ratio on the resulting structures. Unexpectedly, increasing the M:L ratio to more than 1:1 leads to the formation of  $\alpha\text{-Mg}_3(\text{HCOO})_6$  as a second phase beside Mgbp3dc. The intensities of  $\alpha\text{-Mg}_3(\text{HCOO})_6$  diffractions are much higher in the case of a M:L ratio of 3:1 compared to 2:1. To investigate the formation mechanism of  $\alpha\text{-Mg}_3(\text{HCOO})_6$ , the effect of synthesis temperature has been studied. Hydrothermal reactions with M:L molar ratio of 3:1 were carried out at different temperatures (85, 100, and 120 °C) for 72 h and the mixtures were slowly cooled to room temperature for another 72 h. White precipitates were obtained from all the reactions and their structures were investigated by powder XRD. As shown in Figure 2(b), at both 85 °C and 100 °C amorphous products are formed, indicating that these temperatures are not sufficient for the crystallization process. This could be due to the ionic competition for coordination with bpdc ligands as a result of increasing the  $\text{Mg}^{2+}$  ions concentration that may hinder the crystallization process at these temperatures. A mixture of Mgbp3dc and  $\alpha\text{-Mg}_3(\text{HCOO})_6$  was obtained simulta-

neously at 120 °C. Apparently, a temperature of 120 °C is necessary to generate  $\alpha\text{-Mg}_3(\text{HCOO})_6$ . Herein, the only possible scenario is DMF decomposition under the current hydrothermal conditions into CO and dimethylamine, which plays a crucial role in the formation of formate ions via one of the suggested mechanisms presented in Scheme 1. Therefore, we investigated the effect of reaction time in order to reveal the predominant reaction mechanism for the present conditions. The hydrothermal reactions were carried out for a 3 M:1 L ratio at 120 °C over a reaction period of 24 h, 72 h (naturally cooled down to room temperature), and 72 h followed by a slow cooling for another 72 h (in a total reaction period of 6 days). Surprisingly, the hydrothermal reaction for only 24 h resulted in the formation of a third structure; neither Mgbp3dc nor  $\alpha\text{-Mg}_3(\text{HCOO})_6$  was formed. The XRD pattern of the resulting material has an excellent agreement with that of the perovskite-like  $[\text{Mg}(\text{HCOO})_3][\text{NH}_2(\text{CH}_3)_2]$  framework (PMF). Upon increasing the reaction period to 72 h, the diffraction pattern of Mgbp3dc is observed, indicating that the crystallization of Mgbp3dc requires at least 3 days. Increasing the reaction time by slow cooling leads to the formation of  $\alpha\text{-Mg}_3(\text{HCOO})_6$ , while the Mgbp3dc phase is not affected. These findings suggest mechanism 2 as the predominant pathway in which PMF is formed first, as an early-stage product, and as the reaction proceeds with further DMF decomposition  $\alpha\text{-Mg}_3(\text{HCOO})_6$  is formed. This finding is also consistent with what had been reported by Kravchenko et al.,<sup>[35]</sup> who observed the formation of PMF in the early stage reaction between MgO and formic acid vapor which, in turn, led to the formation of  $\alpha\text{-Mg}_3(\text{HCOO})_6$  as the reaction proceeds.<sup>[35]</sup>

Rossin et al.<sup>[36]</sup> synthesized PMF by reacting Mg salt with formamide in presence of cyclobutane-1,19-dicarboxylic acid. On the other hand,  $\alpha\text{-Mg}_3(\text{HCOO})_6$  could be directly synthesized

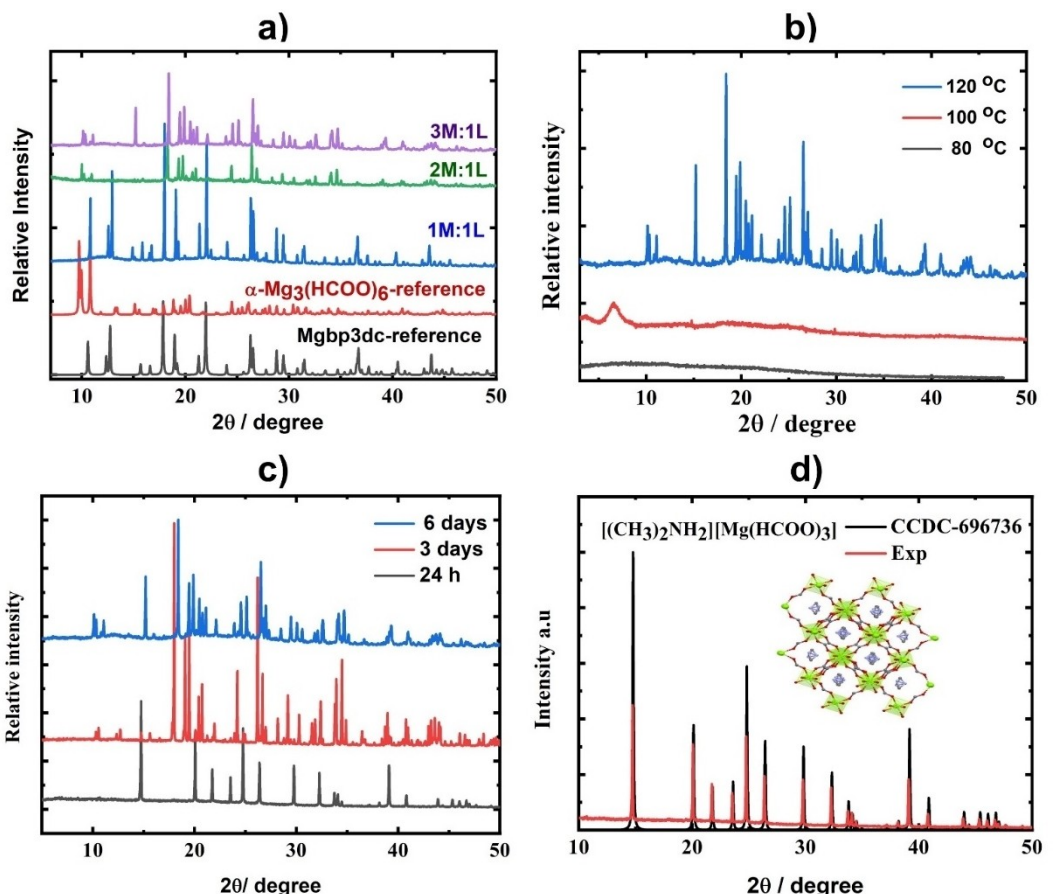


**Figure 2.** Powder XRD showing a) the effect of M:L ratio on the resulting structures compared to the predicted reference cards, b) the effect of the hydrothermal reaction temperatures, c) the effect of hydrothermal reaction time, and d) the as-synthesized material after 24 h compared to the reference card of PMF.

from the hydrothermal reaction of Mg salt and DMF at 130°C for a week, following the reaction mechanism 1 depicted in Scheme 1.<sup>[37]</sup> The aforementioned findings suggest that mechanism 2 is predominant in the presence of carboxylic acid (formic acid or cyclobutane-1,19-dicarboxylic acid), while mechanism 1 is relevant in the absence of carboxylic acid. This also explains the predominance of mechanism 2 in the current work, where the bp3dc ligand plays the same role as cyclobutane-1,19-dicarboxylic acid.

To further confirm the dependency of the reaction mechanism on the presence of carboxylic acid and the possibility of  $\alpha\text{-Mg}_3(\text{HCOO})_6$  formation under the hydrothermal reaction at 120°C, the reactions of Mg salt with DMF in absence and presence of formic acid (as a direct source of formate ions) were carried out. In both cases cubic crystals of  $\alpha\text{-Mg}_3(\text{HCOO})_6$  were successfully obtained, as demonstrated by the very good agreement of the XRD pattern with reference card (CCDC 1019005) as shown in Figure 3.  $\alpha\text{-Mg}_3(\text{HCOO})_6$  that was formed from DMF decomposition at 120°C, showed higher crystallinity and purity compared to the product obtained in presence of formic acid. The reaction of Mg salt with formic acid in a 1:1 molar ratio in DMF solvent at 100°C for three days leads to the formation of  $\alpha\text{-Mg}_3(\text{HCOO})_6$  with PMF as a second phase, that completely transforms to  $\alpha\text{-Mg}_3(\text{HCOO})_6$  after the thermal

evacuation of the material as shown in Figure 3(b).  $^1\text{H}$  and  $^{13}\text{C}$  NMR have been used to check the purity of  $\alpha\text{-Mg}_3(\text{HCOO})_6$  and to confirm the absence of the PMF phase after thermal evacuation (see Figure S2). This confirmed the proposed reaction mechanisms (see above) of  $\alpha\text{-Mg}_3(\text{HCOO})_6$  formation in absence and presence of carboxylic acid. Additionally, single crystals of  $\alpha\text{-Mg}_3(\text{HCOO})_6$  could be synthesized with very high purity at a lower temperature and shorter reaction time compared to the report in Ref. [37]. It is worth mentioning that all attempts to prepare  $\alpha\text{-Mg}_3(\text{HCOO})_6$  from DMF and Mg salts at 85, 100, and 120°C using screw-capped vials were not successful. Therefore, the autoclave conditions play a crucial role in DMF decomposition at lower temperatures compared to what had been mentioned by Spanopoulos et al.<sup>[37]</sup>

Herein, three different kinds of either single-phase or multi-phases magnesium-based frameworks could be successfully synthesized and isolated by controlling the hydrothermal reaction conditions. Table 1 summarizes the crystallographic information of PMF,  $\alpha\text{-Mg}_3(\text{HCOO})_6$ , Mgpb3dc, and  $\alpha\text{-Mg}_3(\text{HCOO})_6$  in MOF1 obtained after structure refinements.

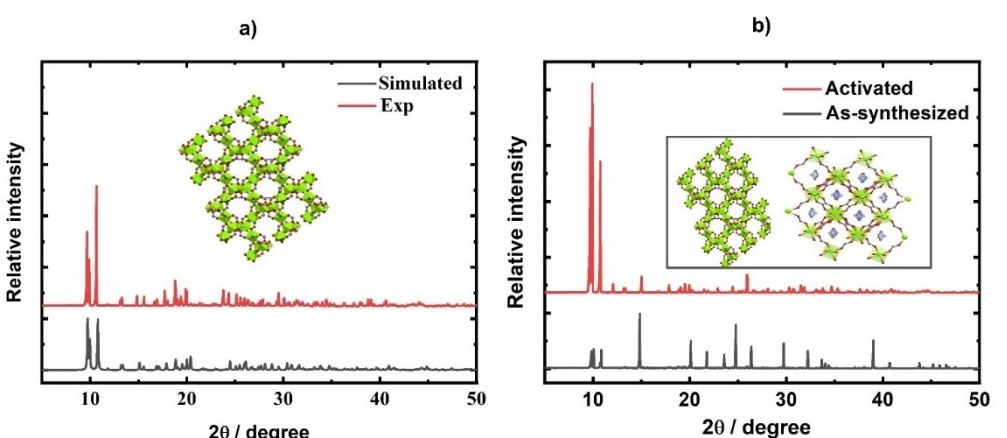
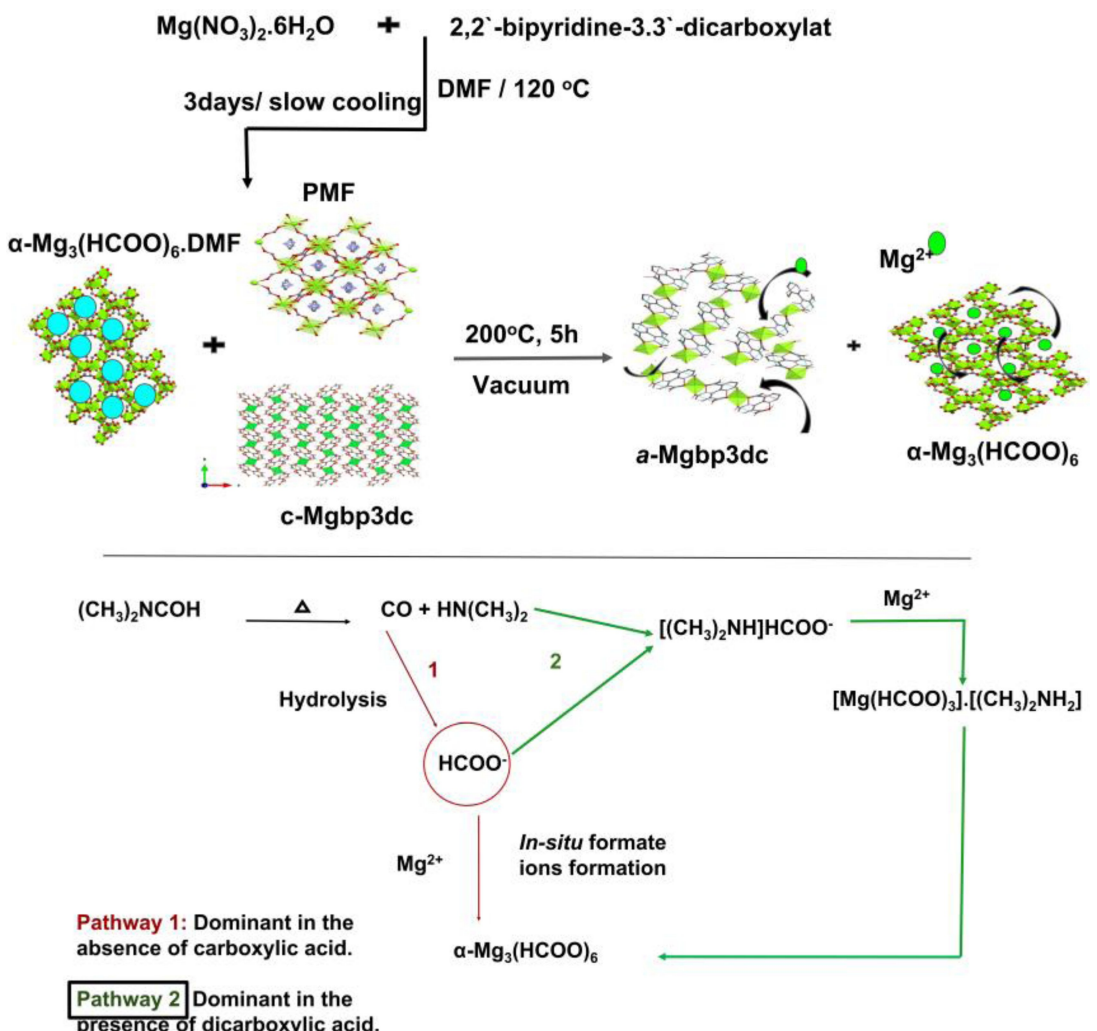


**Figure 3.** XRD of a)  $\alpha\text{-Mg}_3(\text{HCOO})_6$  synthesized in the absence of formic acid by the hydrothermal reaction of 3 mmol Mg salt in 10 mL DMF at 120 °C for 72 h then slow cooling to room for 72 h (Inset: the crystal structure of  $\alpha\text{-Mg}_3(\text{HCOO})_6$ ) and b) as-synthesized  $\alpha\text{-Mg}_3(\text{HCOO})_6$  synthesized in the presence of formic acid and after activation at 150 °C for 24 h (Inset: the crystal structure of  $\alpha\text{-Mg}_3(\text{HCOO})_6$  and PMF).

Structure	Crystal structure	Space group	$\alpha, \beta, \gamma$	Lattice parameters [Å]	Crystal volume [Å <sup>3</sup> ]
Mgbp3dc	Orthorhombic	P 2 <sub>1</sub> 2 <sub>1</sub> 2	$\alpha = \beta = \gamma = 90^\circ$	$a = 13.918$ $b = 6.156$ $c = 8.413$	720.819
<sup>[a]</sup> $\alpha$ -Mg <sub>3</sub> (HCOO) <sub>6</sub>	Monoclinic	P 21/n	$\beta = 91.15^\circ$	$a = 11.381$ $b = 9.919$ $c = 14.615$	1649.860
<sup>[b]</sup> $\alpha$ -Mg <sub>3</sub> (HCOO) <sub>6</sub>	Monoclinic	P 21/n	$\beta = 91.317^\circ$	$a = 11.169$ $b = 9.859$ $c = 14.821$	1632.017
PMF	Tetragonal	R -3 c	$\gamma = 120^\circ$	$a = 8.1698$ $b = 8.1698$ $c = 22.6606$	1512.456
$\alpha$ -Mg <sub>3</sub> (HCOO) <sub>6</sub> in MOF1 after thermal activation	Monoclinic	P 21/n	$\beta = 91.316^\circ$	$a = 11.415$ $b = 9.915$ $c = 14.6577$	1658.954
Mgbp3dc in MOF1 (Before activation)	Orthorhombic	P 2 <sub>1</sub> 2 <sub>1</sub> 2	$\alpha = \beta = \gamma = 90^\circ$	$a = 13.845$ $b = 6.0674$ $c = 8.423$	707.558

<sup>[a]</sup> synthesized in the presence of formic acid. <sup>[b]</sup> synthesized from DMF decomposition.

### $\alpha$ -Mgbp3dc / $\alpha$ -Mg<sub>3</sub>(HCOO)<sub>6</sub> mixtures

To further characterize  $\alpha$ -Mgbp3dc/ $\alpha$ -Mg<sub>3</sub>(HCOO)<sub>6</sub> mixtures, the effect of thermal activation and evacuation was investigated by PXRD, TGA, NMR, and mass-spectroscopy. As shown in Figure S3(a), after thermal activation the diffraction peaks of  $\alpha$ -Mg<sub>3</sub>(HCOO)<sub>6</sub> became predominant. The diffraction pattern of Mgbp3dc completely disappeared as a result of the thermal amorphization as already shown in Figure 1. On the other hand, the intensity of  $\alpha$ -Mg<sub>3</sub>(HCOO)<sub>6</sub> diffraction peaks increased sharply as an indication of the enhanced crystallinity after the evacuation and activation processes. As shown in Figure S3(b), there are no observed PMF diffraction peaks after thermal evacuation indicating the transformation of PMF into  $\alpha$ -Mg<sub>3</sub>(HCOO)<sub>6</sub> as a result of further decomposition of the guest DMF molecules.

Based on the aforementioned results, PMF undergoes a structural transformation to  $\alpha$ -Mg<sub>3</sub>(HCOO)<sub>6</sub> in presence of a high formate ion concentration as a result of DMF decomposition during the evacuation process. Mass spectroscopy was used to further confirm the previous assumption and to confirm the presence of Mgbp3dc and  $\alpha$ -Mg<sub>3</sub>(HCOO)<sub>6</sub>. It is noticed that the molecular peak of PMF at  $m/z = 205.46$  disappeared after thermal activation as depicted in Figure 4(a and b).

On the other hand, the molecular peaks of c-Mgbp3d [ $\text{Mg}(\text{bp3dc}\cdot(\text{H}_2\text{O})_4)$ ],  $\alpha$ -Mg<sub>3</sub>(HCOO)<sub>6</sub> and their solvated structures are detected by MS before thermal activation. The molecular peak of  $\alpha$ -Mgbp3dc (dehydrated) as well as  $\alpha$ -Mg<sub>3</sub>(HCOO)<sub>6</sub> and their solvated structures have been detected in the spectra of MOF1 after thermal activation. These findings confirm the presence of MOF1 after thermal activation of a  $\alpha$ -Mg<sub>3</sub>(HCOO)<sub>6</sub> and  $\alpha$ -Mgbp3dc mixture.

Both TGA and NMR have been used to calculate the percentage of  $\alpha$ -Mgbp3dc to  $\alpha$ -Mg<sub>3</sub>(HCOO)<sub>6</sub> in MOF1 as well as to confirm the phase purity. Figure 4(c) shows TGA of MOF1

before and after thermal activation. From differential thermogravimetric analysis (dTGA), it is observed that there are three mass losses in the region from 330 to 450 °C. The first mass loss at 330 °C is related to the decomposition of the  $\alpha$ -Mgbp3dc framework. The second mass loss starting at 400 °C is due to the phase transition from  $\alpha$ -Mg<sub>3</sub>(HCOO)<sub>6</sub> to  $\beta$ -Mg(HCOO)<sub>2</sub>. The mass loss at 440 °C is due to the decomposition of  $\beta$ -Mg(HCOO)<sub>2</sub> to MgO.<sup>[35]</sup> After normalization of the mass loss and the humidity contribution due to air exposure to 100%, the mass loss due to  $\alpha$ -Mgbp3dc is 30.3%, which is equivalent to two  $\alpha$ -Mgbp3dc (calculated 30.9%). The mass loss due to decomposition of  $\alpha$ -Mg<sub>3</sub>(HCOO)<sub>6</sub> to  $\beta$ -Mg(HCOO)<sub>2</sub> and finally to MgO is 42.6%, which is equivalent to 3  $\alpha$ -Mg<sub>3</sub>(HCOO)<sub>6</sub> (calculated 42%).

Therefore, MOF1 is composed of 3  $\alpha$ -Mg<sub>3</sub>(HCOO)<sub>6</sub> and 2  $\alpha$ -Mgbp3dc. The same results have been obtained by <sup>1</sup>H NMR as shown in Supporting Information Figure S4.

The morphology of MOF1 before and after activation has been investigated by SEM as depicted in Figure 5. It is observed that MOF1 as-synthesized showed the presence of mixed morphologies due to the presence of different structures. The morphology of MOF1 is more shaped after thermal activation compared to the as-synthesized material. However, two different morphologies were still observed. The large monoclinic crystals are  $\alpha$ -Mg<sub>3</sub>(HCOO)<sub>6</sub>, while the spongy-crumbled and distorted material is mainly  $\alpha$ -Mgbp3dc.

### Solid electrolytes and ionic conductivity measurements

All the previous reports of MOFs-based SEs are based on the guest-host interaction mechanism to incorporate metal ions into the cavities of the MOFs structures.<sup>[1,24,26]</sup> The main obstacle of this approach is that the maximum amount of incorporated metal salt does not exceed 4.3% and is always accompanied by large amounts of guest solvent molecules, typically in the range

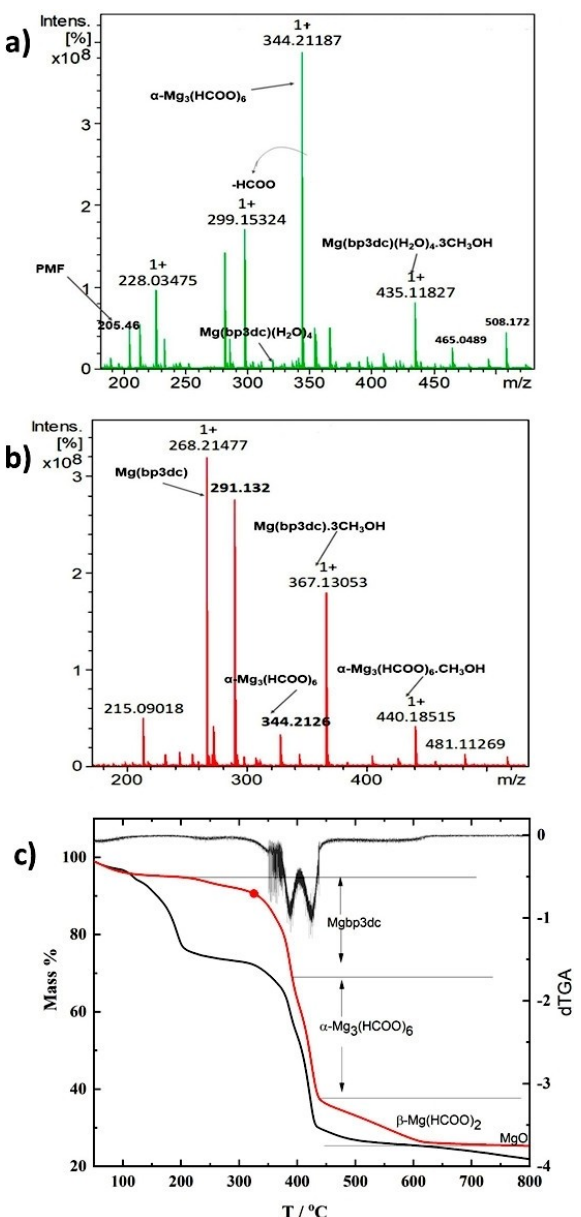


Figure 4. ESI-MS of a) as-synthesized MOF1, b) α-MOF1, and c) TGA and dTGA of MOF1 (black curve) and α-MOF1 (red curve).

of 45–55 wt%.<sup>[1,24]</sup> Herein, we introduce mixed MOFs with two different diffusion pathways and less guest solvent content as a promising SE for Mg-ion batteries. Upon using MOF1 as a matrix for Mg salts,  $Mg^{2+}$  ions will be incorporated into the small cavities of  $\alpha\text{-Mg}_3(\text{HCOO})_6$ , while the presence of  $\alpha\text{-Mgbp3dc}$  offers extra pathways for  $Mg^{2+}$  diffusion. In fact, the amorphization of Mgbp3dc leads to an opening of  $Mg^{2+}$  sites within the framework due to the removal of coordinated water. This helps the Mg salt to coordinate with anions, leaving Mg ions free to move. The ionic conductivity measurements were performed on powder pellets using alternating current electrochemical impedance spectroscopy (EIS) as described in the experimental section. Initially, to provide a proof of concept, the ionic conductivity of  $\alpha\text{-MOF1-Mg(TFSI)}_2\text{-MgCl}_2\text{-G4-10}$  has

been compared to  $\alpha\text{-Mg}_3(\text{HCOO})_6\text{-Mg(TFSI)}_2\text{-MgCl}_2\text{-G4-10}$  at 30 °C. For better clarity, both x and y axes were multiplied by the area/thickness ( $a/l$ ) of the pellets so that the ionic conductivity will be the reciprocal of the right-hand minima. As shown in Figure 6(a and b), the mixed MOFs showed the highest ionic conductivity of  $3.8 \times 10^{-5} \text{ S cm}^{-1}$  compared to  $1.1 \times 10^{-6} \text{ S cm}^{-1}$  of  $\alpha\text{-Mg}_3(\text{HCOO})_6$ . Based on the ionic conductivity results, the increase in the degree of disorder in MOF-based SEs, which is due to mixing two different MOFs, one of which is amorphized, enhances the ionic diffusion of  $Mg^{2+}$  ions. To investigate any possible proton diffusion from the solvated  $\alpha\text{-MOF1}$  or the presence of any electronic conductivity, the ionic conductivity of  $\alpha\text{-MOF1-G4}$  was also measured. The Nyquist plot of  $\alpha\text{-MOF1-G4}$  in Figure 6(c) shows that  $\alpha\text{-MOF1-G4}$  is an ionic and electronic insulator with an ionic conductivity of  $15.1 \times 10^{-10} \text{ S cm}^{-1}$  at 30 °C. From these results, it is confirmed that the reported ionic conductivity is obviously due to  $Mg^{2+}$  ion diffusion.

The effect of the nature of the Mg salt on the ionic conductivity of  $\alpha\text{-MOF1}$ -based SE has also been investigated. As  $Mg(\text{TFSI})_2$  has low ability to form aggregates during the solvation process due to its bulky structure and the highly-delocalized charges of  $\text{TFSI}^-$ , it has been chosen as a primary Mg salt.  $Mg(\text{TFSI})_2\text{-MgCl}_2$  was replaced by  $Mg\text{Cl}_2$ ,  $Mg(\text{TFSI})_2\text{-AlCl}_3$ , and  $Mg(\text{TFSI})_2$ , and EIS were measured at different temperatures from 30–100 °C. Figure 7 shows the EIS of  $\alpha\text{-MOF1-Mg salt-G4}$  at 40 °C. It is shown that  $Mg(\text{TFSI})_2\text{-MgCl}_2\text{-10}$  provides the highest ionic conductivity compared to the others. Surprisingly,  $Mg(\text{TFSI})_2\text{-AlCl}_3\text{-20}$  (10 wt% total Mg salt) showed a decrease in the ionic conductivity compared to 10 wt%  $Mg(\text{TFSI})_2$ . This could be due to the ionic diffusion competition between  $\text{Al}^{3+}$  and  $Mg^{2+}$  ions. The sample with only  $Mg\text{Cl}_2$  did not show any Mg ion diffusion and its ionic conductivity was similar to  $\alpha\text{-MOF1-G4}$  (Figure S9e). This could be due to  $Mg\text{Cl}_2$  has a high tendency to form ion pairs and aggregates in ethereal solution. The presence of  $Mg(\text{TFSI})_2$ , however, facilitates somehow its dissociation. Upon increasing the mass percentage of  $Mg(\text{TFSI})_2\text{-MgCl}_2$  to 20 wt%, the ionic conductivity decreases compared to 10 wt%. Herein,  $\alpha\text{-MOF1-Mg-TFSI}_2\text{-MgCl}_2\text{-G4-10}$  is the optimum combination in this work. The evolution of ionic conductivity as function of temperature for all  $\alpha\text{-MOF1-Mg salt-G4}$  samples showed excellent correlation with an Arrhenius-type behavior. As the temperature increases, the ionic conductivities increase as a result of the enhanced ionic mobility. The calculated activation energies of diffusion are 0.2, 0.22, 0.58, 0.669 eV for  $\alpha\text{-MOF1-Mg(TFSI)}_2\text{-G4-10}$ ,  $\alpha\text{-MOF1-Mg(TFSI)}_2\text{-MgCl}_2\text{-G4-10}$ ,  $\alpha\text{-MOF1-Mg(TFSI)}_2\text{-AlCl}_3\text{-G4-20}$ , and  $\alpha\text{-MOF1-Mg(TFSI)}_2\text{-MgCl}_2\text{-G4-20}$ , respectively. The small values of activation energy reflect the smooth migration of Mg ions through MOFs-based SEs. To investigate any electronic conductivity contributions from  $\alpha\text{-MOF1-Mg-salt-G4}$ , chronoamperometry curves of an  $\alpha\text{-MOF1-Mg(TFSI)}_2\text{-MgCl}_2\text{-G4-10}$  pellets sandwiched between two blocking stainless steel (SS) electrodes have been recorded at 40 °C by applying 0.5 V for 2 h until a steady-state current was achieved as shown in Figure 8(a). The current decays immediately and reaches a steady-state value. The total transport number was calculated to be 0.998

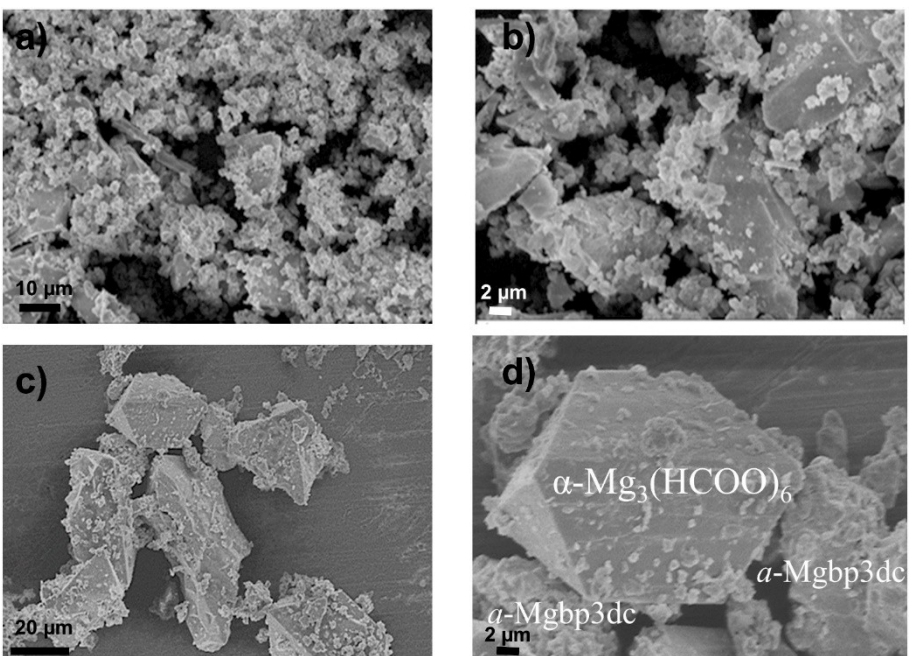


Figure 5. SEM of a and b) the as-synthesized MOF1, and c and d) a-MOF1.

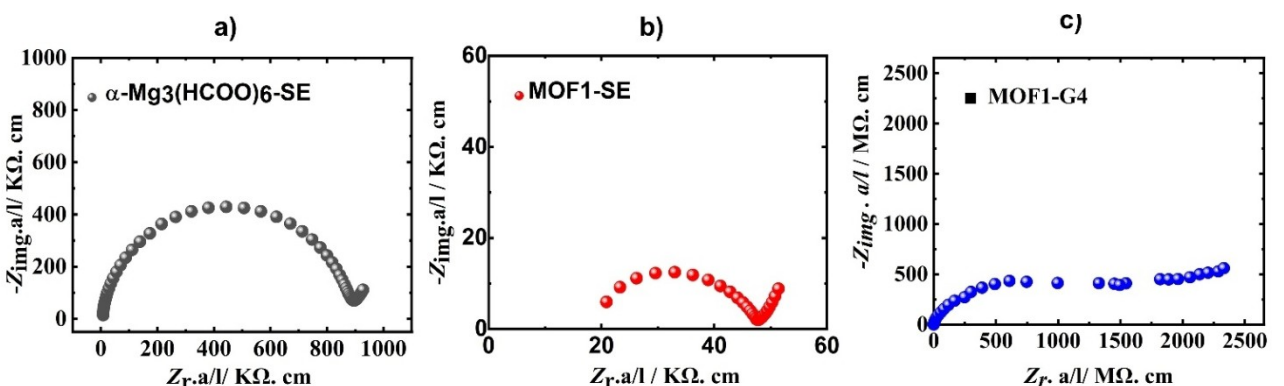


Figure 6. Nyquist plots at 30 °C of a) single phase  $\alpha\text{-Mg}_3(\text{HCOO})_6$ -based SE, b) mixed MOFs-based SE where, 10 wt % (1:1  $\text{MgCl}_2:\text{Mg}(\text{TFSI})_2$ ) were used as Mg salt and G4 was used for solvation, and c) G4 solvated a-MOF1.

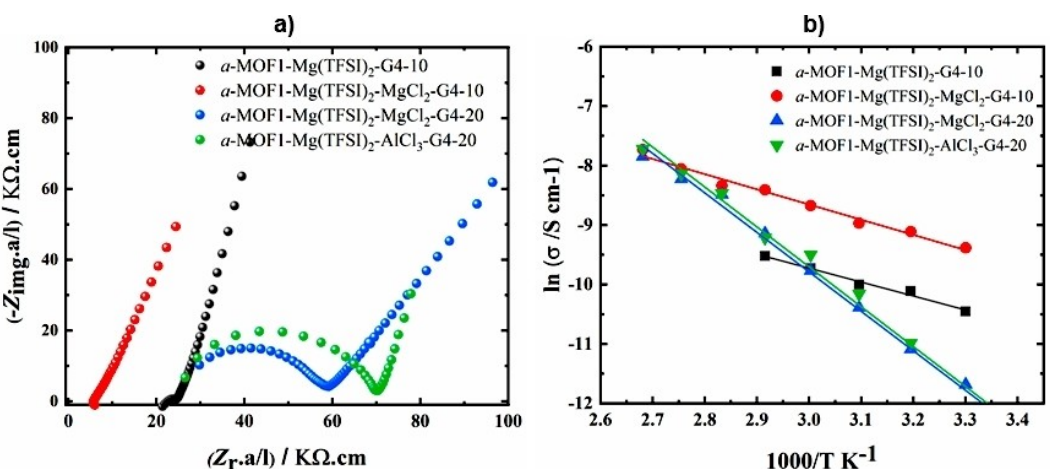
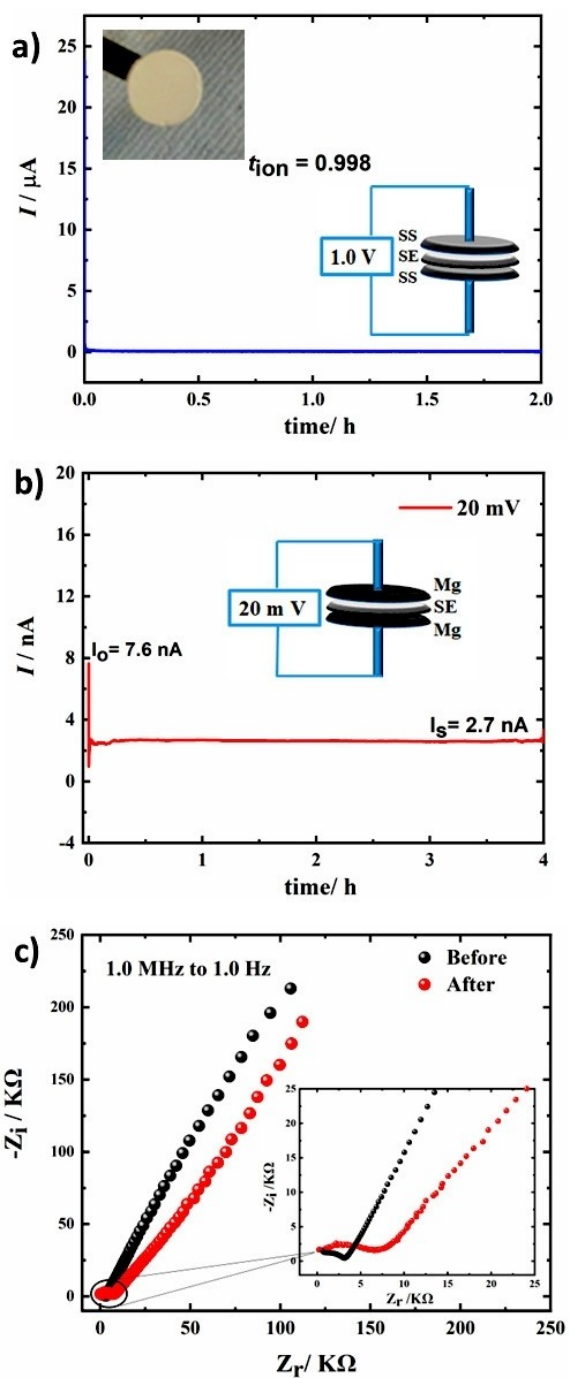


Figure 7. a) Nyquist plots of a-MOF1-based SEs with different Mg salts at 40 °C and b) Arrhenius relation showing the change in ionic conductivity with temperature (slopes have been used to calculate their activation energies of diffusion).



**Figure 8.** a) The recorded  $I/t$  curve at 0.5 V of  $\alpha$ -MOF1-Mg(TFSI)<sub>2</sub>-MgCl<sub>2</sub>-G4-10 SE sandwiched between two SS electrodes, inset: a photograph of SE pellet, b) DC polarization curve at 20 mV of  $\alpha$ -MOF1-Mg(TFSI)<sub>2</sub>-MgCl<sub>2</sub>-G4-10 SE sandwiched between two Mg electrodes, and c) Nyquist plots before and after DC polarization.

that means the conductivity of  $\alpha$ -MOF1-Mg(TFSI)<sub>2</sub>-MgCl<sub>2</sub>-G4-10 is mainly ionic in nature without a significant electronic contribution. XRD, FT-IR, TGA, and <sup>1</sup>H, <sup>13</sup>C, and <sup>19</sup>F NMR were used to investigate the structures of the prepared SEs. The results and their discussion are given in the Supporting Information Figures S5–S8. It is worth mentioning that the solvent percentages in SEs calculated from TGA are in the

range of 20–30 wt%, which is the lowest solvent content among the reported values for MOFs or polymer-based electrolytes ca. 45–55 wt%.<sup>[1]</sup>

### Mg/Mg symmetric cell

The cationic transference number  $t_+$  of  $\alpha$ -MOF1-Mg(TFSI)<sub>2</sub>-MgCl<sub>2</sub>-G4-10 was determined by assembling a symmetric Mg/SE/Mg cell and by combining the results of DC polarization with AC EIS experiments using the Vincent-Bruce method.<sup>[38]</sup> An initial AC EIS was recorded for the freshly assembled cell then a very small DC polarization voltage was applied (20 mV) for 3–4 h until a steady-state current was achieved, followed by repeating the AC EIS measurement, again after the polarization. The initial and steady-state currents were recorded from the DC polarization experiment while the initial resistance and the resistance after polarization were recorded from EIS measurements. It is worth mentioning that in many studies, especially those using polymer-based SEs, voltages of 0.3 to 1.0 V are applied to calculate  $t_+$ , herein the ions will move by means of diffusion that results in a positive error in calculating the cationic transference number. The higher the voltage value, the higher the diffusion, and consequently the higher the positive error. Therefore, it is crucial to only apply a very small voltage value which should not exceed 30 mV in order to avoid the diffusion of ions by means of voltage instead of their migration. Figure 8 shows the current-time curve and Nyquist plots before and after the polarization for  $\alpha$ -MOF1-Mg(TFSI)<sub>2</sub>-MgCl<sub>2</sub>-G4-10. The calculated  $t_+$  is 0.335 indicating the smooth migration of Mg<sup>2+</sup> ions inside  $\alpha$ -MOF1-Mg(TFSI)<sub>2</sub>-MgCl<sub>2</sub>-G4-10 SE. In fact, the diffusion of Mg<sup>2+</sup> ions within solids is inherently slow due to its high charge density. Taking into account that the charge of the Mg<sup>2+</sup> ion is twice larger than that of the Li<sup>+</sup> ion, although the ionic radius of Mg<sup>2+</sup> (0.72 Å) is close to that of Li<sup>+</sup> (0.76 Å).<sup>[39]</sup> This slows the kinetics of Mg<sup>2+</sup> and results in a higher migration barrier for Mg<sup>2+</sup> compared to Li<sup>+</sup> ions. However, this value is also comparable to what is reported for polymer-based SEs despite the use of a relatively high applied voltages.<sup>[40]</sup>

The cyclic voltammogram of the Mg/ $\alpha$ -MOF1-Mg(TFSI)<sub>2</sub>-MgCl<sub>2</sub>-G4-10/Mg cell at a scan rate of 0.5 mV s<sup>-1</sup> is depicted in Figure 9(a), showing Mg deposition/dissolution peaks at -1.5 and 2.0 V vs. Mg/Mg<sup>2+</sup>, respectively. This high overpotential is due to the relatively low conductivity of SE compared to non-aqueous liquid electrolytes. In order to test the stability of SE in the presence of Mg electrodes and the feasibility of using  $\alpha$ -MOF1-Mg(TFSI)<sub>2</sub>-MgCl<sub>2</sub>-G4-10 SE as a promising SE, Mg was deposited for 10 h after which repeated galvanostatic deposition/stripping cycles were performed at 0.1  $\mu$ A cm<sup>-2</sup> for nine successive cycles. For each cycle, 10 h were used for the deposition and stripping process (total 20 h cycle<sup>-1</sup>). It is obvious from Figure 9(b) that the reversibility of the Mg deposition/stripping process is enhanced upon cycling which is also confirmed from the CV after the galvanostatic experiment. The CV after galvanostatic cycling showed a great enhancement in both the reversibility and the current of Mg deposition and stripping processes compared to the initially

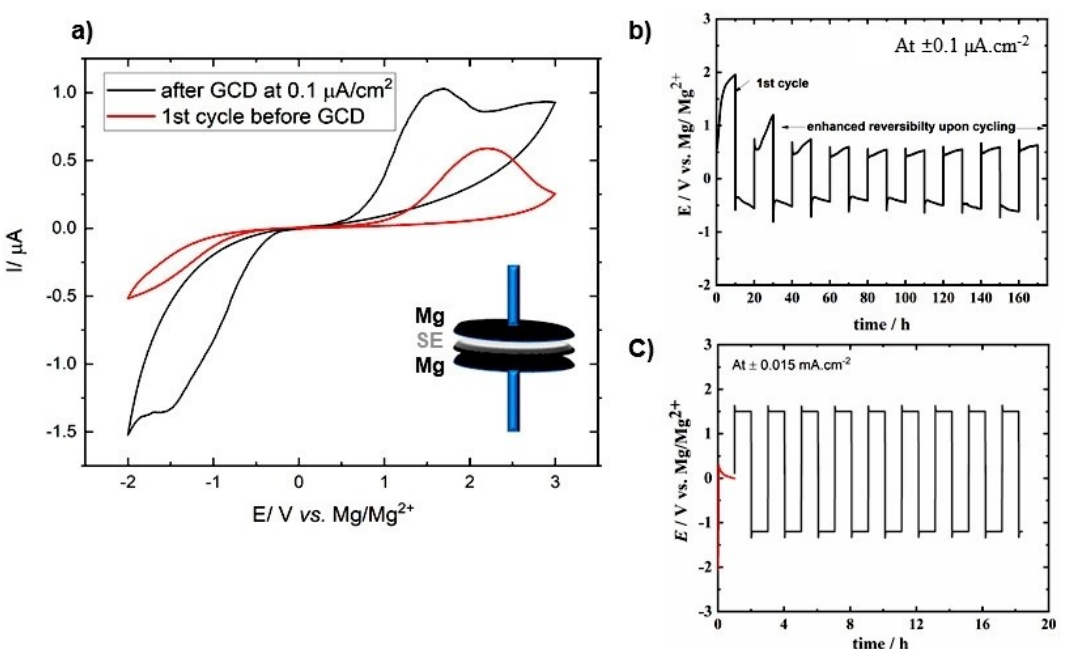


**Figure 9.** a) CV of Mg/ $\alpha$ -MOF1-Mg(TFSI)<sub>2</sub>-MgCl<sub>2</sub>-G4-10 SE/Mg before and after galvanostatic cycling, b) galvanostatic cycling at  $0.1 \mu A \cdot cm^{-2}$  for 20 h cycle $^{-1}$  and c) galvanostatic cycling at  $0.015 \text{ mA} \cdot \text{cm}^{-2}$  for 2 h cycle $^{-1}$ .

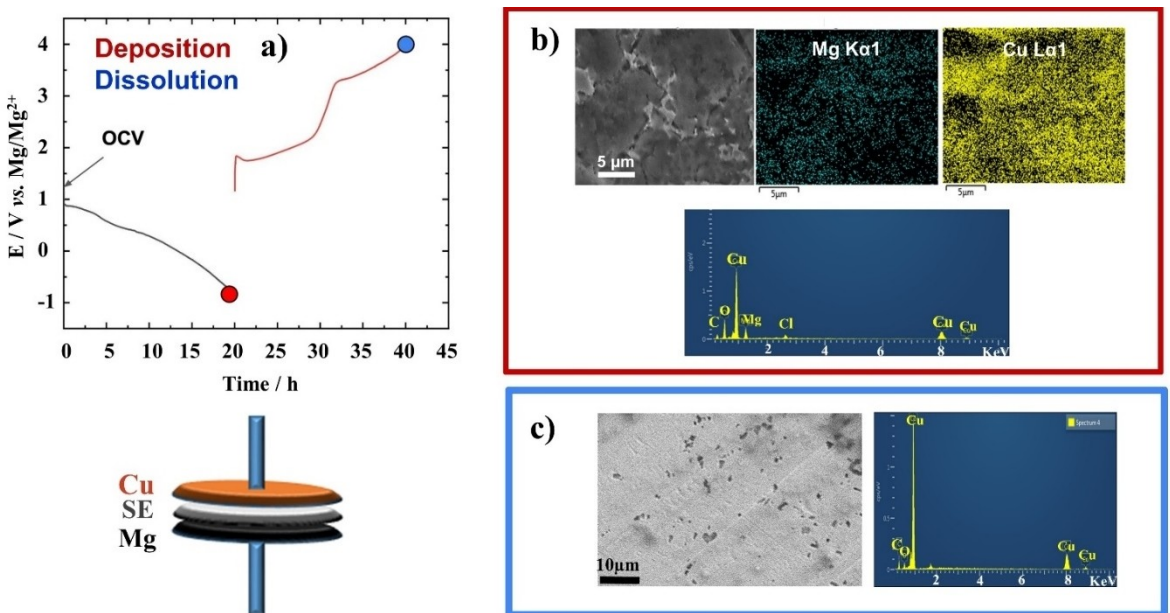


**Figure 10.** a) Galvanostatic curve of Mg deposition/dissolution at  $0.7 \mu A \cdot cm^{-2}$  for 20 h deposition and 20 h dissolution, b) the post-mortem SEM, elemental mapping and EDS after Mg deposition and c) the post-mortem SEM and its corresponding EDS after Mg dissolution.

recorded CV. The enhancement in the reversibility with cycling could be due to the removal of the residual oxides from the Mg surface upon cycling. Even after 170 h of successive deposition/stripping processes,  $\alpha$ -MOF1-Mg(TFSI)<sub>2</sub>-MgCl<sub>2</sub>-G4-10 SE still enables Mg<sup>2+</sup> deposition/stripping. This proves the feasibility of using  $\alpha$ -MOF1-Mg(TFSI)<sub>2</sub>-MgCl<sub>2</sub>-G4-10 SE as a promising SE for Mg-ion batteries and its excellent stability in the presence of a metallic Mg anode. It is worth mentioning here that, as a result of the relatively low ionic conductivity of  $\alpha$ -MOF1-

Mg(TFSI)<sub>2</sub>-MgCl<sub>2</sub>-G4-10 SE compared to the liquid electrolyte, the observed currents of Mg deposition and stripping in CVs are relatively low and, consequently, a low current density was used for the galvanostatic tests. However, upon increasing the current density to  $0.015 \text{ mA} \cdot \text{cm}^{-2}$ , the reversible Mg deposition/stripping is still observed with an increase in the overpotential. The stability of  $\alpha$ -MOF1-Mg(TFSI)<sub>2</sub>-MgCl<sub>2</sub>-G4-10 SE was further investigated by tracking structural or morphological changes

for  $\alpha$ -MOF1-Mg(TFSI)<sub>2</sub>-MgCl<sub>2</sub>-G4-10 pellets before and after cycling by SEM and XRD.

As shown in Figure S10(a and b), the morphology of the SE before and after cycling did not change significantly; however, we observe a reduction in the particle size after cycling compared to the freshly-prepared SE, which is certainly a consequence of their pressing and grinding. The XRD patterns of fresh  $\alpha$ -MOF1-Mg(TFSI)<sub>2</sub>-MgCl<sub>2</sub>-G4-10 powder and the pellet after galvanostatic cycling are depicted in Figure S10(c). No significant change in the structure has been observed, indicating that the  $\alpha$ -MOF1-Mg(TFSI)<sub>2</sub>-MgCl<sub>2</sub>-G4-10 SE has a high structural integrity capable of sustaining both the high pressure used for pellet preparation as well as the electrochemical cycling.

### Mg deposition on Cu

Mg deposition/stripping was also investigated in an asymmetric Cu/Mg cell by SEM/EDS. SEM and EDS of Cu foil after Mg deposition at  $-0.7 \mu\text{A cm}^{-2}$  for 20 h at 40 °C showed a reversible Mg deposition and dissolution on Cu as depicted in Figure 10(b-d). A pitting corrosion has been observed at the Cu electrode after the dissolution process that could be due to Cu oxidation. These first results provide a good proof of the feasibility of using Mg(TFSI)<sub>2</sub>-MgCl<sub>2</sub>-G4-10 as SE for Mg ion batteries. However, more experimental work is currently in progress in order to further improve the room temperature ionic conductivity of MOF-based semi-SE and to test them with high voltage cathode materials.

## Conclusion

In this work, we presented a strategy to synthesize mixed MOFs with different structures and thermal stabilities in one pot. It was found that hydrothermal reaction conditions have a significant impact on the resulting structure of MOFs. In addition, one should consider the decomposition of the DMF solvent when using the hydrothermal method for MOF synthesis, which affects greatly the resulting structure. Upon thermal activation of this mixture, Mgbp3dc underwent thermal amorphization as a result of the removal of coordinated water molecules, while  $\alpha$ -Mg<sub>3</sub>(HCOO)<sub>6</sub> retained its crystallinity. This step resulted in an opening of Mg<sup>2+</sup> sites within the framework, which helped the added Mg salt to coordinate with anions, leaving Mg ions free to move. Mg semi-SEs based have been synthesized by mixing  $\alpha$ -MOF1 with different Mg salts in G4 followed by excess solvent evaporation. Among the studied semi-SEs,  $\alpha$ -MOF-Mg(TFSI)<sub>2</sub>-MgCl<sub>2</sub>-10 showed an order of magnitude improved ionic conductivity ( $3.8 \times 10^{-5} \text{ S cm}^{-1}$ ) compared to single-phase  $\alpha$ -Mg<sub>3</sub>(HCOO)<sub>6</sub>-Mg(TFSI)<sub>2</sub>-MgCl<sub>2</sub>-10 ( $1.1 \times 10^{-6} \text{ S cm}^{-1}$ ). This  $\alpha$ -MOF-Mg(TFSI)<sub>2</sub>-MgCl<sub>2</sub>-10 semis-SE showed an activation energy for ion diffusion of only 0.22 eV and  $t_{+}$  value of 0.335. Furthermore, it showed enhanced Mg deposition/stripping processes with subsequent galvanostatic cycling. Here, one can conclude that

mixing different MOFs and structure amorphization are ways to improve the ionic conductivities of MOF-based solid electrolytes. Finally, it is worth noting that this is the first work investigating the systematic feasibility of using MOFs-based semi-SEs in Mg batteries, including the electrolyte stability in the presence of Mg metal and its cyclability.

## Experimental Section

### Chemicals and materials

Mg(NO<sub>3</sub>)<sub>2</sub>·6H<sub>2</sub>O (99.999 % trace metals basis), 2,2'-bipyridine-3,3'-dicarboxylic acid (bpdc) (97%), and anhydrous dimethylformamide (DMF) (98.8%) were purchased from Sigma Aldrich and have been used as received. Mg(TFSI)<sub>2</sub>, anhydrous MgCl<sub>2</sub>, and anhydrous AlCl<sub>3</sub> were purchased from Sigma Aldrich and were dried under vacuum at 120 °C before being stored in an Ar-glove box for further use. Tetraglyme (G4) ( $\geq 99\%$ ) was purchased from Sigma Aldrich and was dried with molecular sieves, 4 Å. Mg foils (99.99 % metal basis, thickness = 0.025 mm) and Cu foils ( $\geq 99.9\%$ , thickness 0.015 mm) were obtained from Alfa Aesar.

### Synthesis of Mgbp3dc

#### Single-phase Mg(bp3dc)(H<sub>2</sub>O)<sub>4</sub>

Mg(bpdc)(H<sub>2</sub>O)<sub>4</sub> was synthesized following the approach described in Ref. [33] where 0.5 mmol Mg(NO<sub>3</sub>)<sub>2</sub>·6H<sub>2</sub>O was stirred with 0.5 mmol bp3dc ligands in 10 mL dehydrated DMF until complete dissolution. Afterward, the solution was heated in a Teflon-lined stainless-steel autoclave at 100 °C for 3 days. Here, it is crucial to mention that the mixture was left to slowly evaporate at room temperature for three weeks to obtain the crystals. The powder form of Mg(bpdc)(H<sub>2</sub>O)<sub>4</sub> was prepared by increasing the concentration of the precursors to 1 mmol each in 10 mL DMF and the reaction temperature to 120 °C. Herein, a white gelatinous precipitate is formed which was collected by centrifugation at 9000 rpm and washed at least three times with hot DMF. The resulting material was dried overnight at 80 °C to form the as-synthesized Mg(bpdc)(H<sub>2</sub>O)<sub>4</sub> (DMF).

#### Effect of hydrothermal conditions

To study the effect of synthesis conditions on the structure of Mgbp3dc, different molar ratios of 1:1, 2:1, and 3:1 of Mg<sup>2+</sup> ions:bp3dc ligand were mixed in 10–20 mL anhydrous DMF per 1.0 mmol ligand until complete dissolution. Afterwards, the solutions were distributed in 50 mL Teflon-lined stainless-steel autoclaves and heated up to 80–120 °C for 24–72 h. They were then left to naturally cool down to room temperature or at a cooling rate of 1.3 °C h<sup>-1</sup>. White gelatinous precipitates are formed in all cases which were collected by centrifugation at 9000 rpm and washed at least three times by hot DMF. The resulting material was dried overnight at 80 °C to form the as-synthesized materials.

#### Synthesis of single phase $\alpha$ -Mg<sub>3</sub>(HCOO)<sub>6</sub>

$\alpha$ -Mg<sub>3</sub>(HCOO)<sub>6</sub> has been prepared by the hydrothermal method in both absence and presence of formic acid. In the absence of formic acid, 3.0 mmol of Mg salt was dissolved in 10 mL DMF followed by hydrothermal reaction at 120 °C for 72 h and slow cooling to room temperature for 72 h. While in the presence of formic acid, 0.77 g

Mg salt was mixed with 0.23 mL formic acid in 10 mL DMF solvent followed by a hydrothermal reaction at 110 °C for 72 h.

### Surface, structural and spectral characterization

Elemental analyses of C, H, and N were obtained from CHN(S) analyser by Elementar vario MICRO cube. Mg percentages in the samples were obtained by inductive coupled plasma atomic emission spectroscopy (ICP-AES) using a Horiba Jovin Yvon Ultima 2 analyser. The samples were dissolved in H<sub>2</sub>O and diluted to a known volume before the measurements. Attenuated total reflection Fourier transform infrared (ATR-FT-IR) spectra of the samples were recorded by Thermo-Scientific Nicolet 6700 FT-IR from 550 to 3000 cm<sup>-1</sup>. For each spectrum, 32 scans were recorded. Thermogravimetric analysis (TGA) data were collected with a TGA/SDTA 851e from Mettler Toledo under N<sub>2</sub> atmosphere from room temperature to 600 or 800 °C with a heating rate of 5 °C min<sup>-1</sup>. Powder diffraction X-ray (PXRD) was recorded on STOE Stadi P diffractometer under the following conditions: 40 kV, 40 mA, CuK $\alpha$  radiation ( $\lambda = 0.154$  nm) using the transmission mode. The powders of solid electrolytes were assembled in the sample holder inside the glovebox to avoid contamination from air. X'pert PANalytical's Highscore software was used for PXRD pattern analyses and Fullprof Suite software for structural refinements. The scanning electron microscope (SEM) images and energy dispersive X-ray spectroscopy (EDS) were carried out using Zeiss LEO 1550 VP field emission SEM (FE-SEM Carl Zeiss, Germany). For nuclear magnetic resonance (NMR) analyses, the samples were digested in D<sub>2</sub>O and sometimes heating was required for complete solubility. <sup>1</sup>H and <sup>13</sup>C NMR spectra were recorded on NMR Bruker 400 MHz (NMR Bruker 500 MHz was used for analysis of Mgbp3dc MOF) and analyzed by MNOVA software. Electrospray Ionization-Mass spectroscopy (ESI-MS) was recorded by Bruker SolariX MS and used to measure the mass spectra of MOF1 before and after thermal activation with fewer fragmentation possibilities. The samples were dissolved in methanol before the measurements.

### Preparation of solid electrolytes (SE1X)

In an Ar-filled glovebox, solid electrolytes were prepared by dispersing  $\alpha$ -MOF1 ( $\alpha$ -Mg<sub>3</sub>(HCOO)<sub>6</sub>- $\alpha$ -Mgbp3dc) and Mg salts in tetraglyme (G4) under a continuous stirring for 48 h. Afterwards, the excess G4 was evaporated and SEs were subjected to vacuum drying at 80 °C overnight under 10 mbar. This method has been used to minimize the solvent extent in MOF-based SEs. SEs used in this study as well as Mg salt compositions and percentages are summarized in Table 2. To investigate any ionic conductivities that might come from the solvated MOF,  $\alpha$ -MOF1 was dispersed in G4 in the same way without the addition of Mg salts.

### Electrochemical characterization

To determine the ionic conductivities electrochemical impedance spectroscopy (EIS) spectra were collected by a Solartron potentiostat equipped with Impedance Analyser (1287 A-1260 A). Cyclic voltammograms (CV), galvanostatic discharging-charging tests (GCD), and EIS between the tests were recorded by a Biologic VMP3 multichannel potentiostat at 40 °C in a thermostatic climate chamber with a maximum deviation of  $\pm 1$  °C unless mentioned. All the cells were left at open circuit voltage (OCV) for 24 h before the measurements except for the single phase  $\alpha$ -Mg<sub>3</sub>(HCOO)<sub>6</sub>-based SEs, the cells were left for 4 days before the measurements until a stable EIS was obtained. SE pellets were sandwiched between two Mg foils (thickness = 0.025 mm, Ø12 mm, Alfa Aesar) for symmetric cell measurements or between Mg foil as a counter electrode and Cu foil (thickness = 0.015 mm, Ø12 mm) as a working electrode for asymmetric cell measurements.

### Ionic conductivity measurements

In an Ar-filled glove box, 0.1 g of the SEs powder was dispensed between two stainless steel discs into a cylindrical PEEK home-made-cell with an inner diameter of 13 mm. The loaded material was then pressed at 5.2 tons for three minutes prior to the thickness measurements by a thickness gauge accurate to 0.2  $\mu$ m. The thickness of the formed pellets was between 0.45 to 0.58 mm. Prior to the electrochemical tests, the cell with the SE pellet was hosted in a stainless-steel case with an upper screw applying a force to the upper part to ensure the electrical contact and stable mechanical stability of the cell. The whole-cell was further sealed in an aluminum bag filled with Ar to avoid any possible exposure to air. AC impedance spectroscopy was used for the conductivity measurements at a temperature range between 25 to 100 °C. The cells were kept at each temperature for two to three hours before each measurement. The EIS spectra were collected at 10 mV AC amplitude with a frequency range between 1 MHz to 100 or 1000 Hz, with 10 points per decade (except for  $\alpha$ -MOF1-G4, 100 mV AC amplitude was used). The SE pellets resistances were determined from the second minima of the semicircle in Nyquist plots. Afterwards, the bulk conductivities were calculated as:

$$\sigma = \frac{I}{R_s A}$$

where  $\sigma$  is the bulk conductivity in S cm<sup>-1</sup>,  $I$  is the pellet thickness in cm,  $R_s$  is the SE pellet resistance in Ohms and  $A$  is the pellet area in cm<sup>2</sup>. Pseudo-activation energies were calculated from Nernst-Einstein equation:<sup>[41]</sup>

$$\sigma = \sigma_0 e^{\frac{-E_a}{k_B T}}$$

**Table 2.** The compositions and percentages of Mg salts added to  $\alpha$ -MOF1 for Mg-SEs preparation.

Solid electrolyte	Percentage of $\alpha$ -MOF1	Volume of G4 [mL]/0.2 g of solid	Percentage and composition f Mg salts	Total percentage of Mg salts
$\alpha$ -MOF1-G4	100%	1.0	0% Mg salt	0%
$\alpha$ -MOF1-Mg(TFSI) <sub>2</sub> -G4-10	90%	1.0	10% Mg(TFSI) <sub>2</sub>	10%
$\alpha$ -MOF1-Mg(TFSI) <sub>2</sub> -MgCl <sub>2</sub> -G4-10	90%	1.0	5% Mg(TFSI) <sub>2</sub> + 5% MgCl <sub>2</sub>	10%
$\alpha$ -MOF1-Mg(TFSI) <sub>2</sub> -AlCl <sub>3</sub> -G4-20	80%	1.0	10% Mg(TFSI) <sub>2</sub> + 10% AlCl <sub>3</sub>	10%
$\alpha$ -MOF1-MgCl <sub>2</sub> -G4-10	90%	1.0	10% MgCl <sub>2</sub>	10%
$\alpha$ -MOF1-Mg(TFSI) <sub>2</sub> -MgCl <sub>2</sub> -G4-20	80%	1.0	10% Mg(TFSI) <sub>2</sub> + 10% MgCl <sub>2</sub>	20%

where  $\sigma_0$  is the pre-exponential factor,  $T$  is the absolute temperature in K,  $E_a$  is the pseudo-activation energy of diffusion and  $k_B$  is Boltzmann constant.

### Total transport and transference number measurements

For total transport number calculation, SE pellets were sandwiched between two ion blocking stainless steel discs of 13 mm diameter before applying a DC potential of 0.5 V for 3 or 4 hours until a steady-state current was achieved. Total ion transport was measured by:

$$t_{\text{ion}} = \frac{I_0 - I_s}{I_0}$$

where  $I_0$  is the initial current (at  $t=0$ ),  $I_s$  is the steady-state current and  $t_{\text{ion}}$  is ion transport number. Mg<sup>2+</sup> ion transference number ( $t_+$ ) was determined by coupling the AC EIS test with the DC polarization experiment, SE pellets were sandwiched between two non-blocking Mg foils. A small constant potential bias  $\Delta V=0.03$  V was applied, and the current was recorded vs. time until a steady-state current was obtained. EIS measurements were carried out before and after DC polarization, then  $t_+$  was calculated by the Bruce and Vincent equation.<sup>[38]</sup>

### Acknowledgements

The authors gratefully acknowledge support by the Deutsche Forschungsgemeinschaft (DFG, German Research Foundation) through research unit FOR-5065 – project number 428906592 and the priority program SPP-2248 – project number 441209207. The authors also would like to thank Prof. Dr. Stefano Passerini for being able to use his group's infrastructure facilities, and Mr. Christian Tontsch from the Institute of Organic Chemistry at the University of Ulm for NMR measurements. Open Access funding enabled and organized by Projekt DEAL.

### Conflict of Interest

The authors declare no conflict of interest.

### Data Availability Statement

Data can not be shared.

**Keywords:** Mg-ion diffusion · Mg-ion battery · MOFs · post-lithium-ion batteries · semi-solid electrolytes

- [1] M. L. Aubrey, R. Ameloot, B. M. Wiers, J. R. Long, *Energy Environ. Sci.* **2014**, *7*, 667.
- [2] R. S. Kumar, M. Raja, M. A. Kulandainathan, A. M. Stephan, *RSC Adv.* **2014**, *4*, 26171.
- [3] J. Wu, X. Guo, *Small* **2019**, *15*, 1804413.

- [4] H. Chen, S.-Y. Han, R.-H. Liu, T.-F. Chen, K.-L. Bi, J.-B. Liang, Y.-H. Deng, C.-Q. Wan, *J. Power Sources* **2018**, *376*, 168.
- [5] A. Rossin, A. Ienco, F. Costantino, T. Montini, B. Di Credico, M. Caporali, L. Gonsalvi, P. Fornasiero, M. Peruzzini, *Cryst. Growth Des.* **2008**, *8*, 3302.
- [6] M. Mączka, A. Ciupa, A. Gagor, A. Sieradzki, A. Pikul, B. Macalik, M. Drozd, *Inorg. Chem.* **2014**, *53*, 5260.
- [7] S. Natarajan, P. Mahata, *Chem. Soc. Rev.* **2009**, *38*, 2304.
- [8] V. Guillerm, D. Kim, J. F. Eubank, R. Luebke, X. Liu, K. Adil, M. S. Lah, M. Eddaoudi, *Chem. Soc. Rev.* **2014**, *43*, 6141.
- [9] Y. Sun, H.-C. Zhou, *Sci. Technol. Adv. Mater.* **2015**, *16*, 054202.
- [10] C. McKinstry, E. J. Cussen, A. J. Fletcher, S. V. Patwardhan, J. Sefcik, *Cryst. Growth Des.* **2013**, *13*, 5481.
- [11] W. Xu, W. Li, L. Lu, W. Zhang, J. Kang, B. Li, *J. Solid State Chem.* **2019**, *279*, 120950.
- [12] X. Cheng, A. Zhang, K. Hou, M. Liu, Y. Wang, C. Song, G. Zhang, X. Guo, *Dalton Trans.* **2014**, *43*, 44944505.
- [13] A. R. Millward, O. M. Yaghi, *J. Am. Chem. Soc.* **2005**, *127*, 17998.
- [14] J. L. C. Rowsell, O. M. Yaghi, *Angew. Chem. Int. Ed.* **2005**, *44*, 4670.
- [15] J. Jiang, H. Furukawa, Y. B. Zhang, O. M. Yaghi, *J. Am. Chem. Soc.* **2016**, *138*, 10244.
- [16] Y. Ozawa, N. Ogihara, M. Hasegawa, O. Hiruta, N. Ohba, Y. Kishida, *Commun. Chem.* **2018**, *1*, 65.
- [17] D. Feng, T. Lei, M. R. Lukatskaya, J. Park, Z. Huang, M. Lee, L. Shaw, S. Chen, A. A. Yakovenko, A. Kulkarni, J. Xiao, K. Fredrickson, J. B. Tok, X. Zou, Y. Cui, Z. Bao, *Nat. Energy* **2018**, *3*, 30.
- [18] Z. Wu, J. Xie, Z. J. Xu, S. Zhang, Q. Zhang, *J. Mater. Chem. A* **2019**, *7*, 4259.
- [19] Z. Zhang, K. Awaga, *MRS Bull.* **2016**, *41*, 883.
- [20] S. Bai, X. Liu, K. Zhu, S. Wu, H. Zhou, *Nat. Energy* **2016**, *1*, 16094.
- [21] Y. Mao, G. Li, Y. Guo, Z. Li, C. Liang, X. Peng, Z. Lin, *Nat. Commun.* **2017**, *8*, 14628.
- [22] A. E. Baumann, D. A. Burns, B. Liu, V. S. Thoi, *Commun. Chem.* **2019**, *2*, 1.
- [23] S. Fischer, J. Roeser, T. C. Lin, R. H. DeBlock, J. Lau, B. S. Dunn, F. Hoffmann, M. Fröba, A. Thomas, S. H. Tolbert, *Angew. Chem. Int. Ed.* **2018**, *57*, 16683.
- [24] S. S. Park, Y. Tulchinsky, M. Dinca, *J. Am. Chem. Soc.* **2017**, *139*, 13260.
- [25] E. M. Miner, S. S. Park, M. Dinca, *J. Am. Chem. Soc.* **2019**, *141*, 4422.
- [26] K. Fujie, K. Otsubo, R. Ikeda, T. Yamada, H. Kitagawa, *Chem. Sci.* **2015**, *6*, 4306.
- [27] B. M. Wiers, M. L. Foo, N. P. Balsara, J. R. Long, *J. Am. Chem. Soc.* **2011**, *133*, 14522.
- [28] S. Ikeda, M. Takahashi, J. Ishikawa, K. Ito, *Solid State Ionics* **1987**, *23*, 125.
- [29] S. Higashi, K. Miwa, M. Aoki, K. Takechi, *Chem. Commun.* **2014**, *50*, 1320.
- [30] E. Roedern, R.-S. Kühnel, A. Remhof, C. Battaglia, *Sci. Rep.* **2017**, *7*, 1.
- [31] P. Canepa, S. H. Bo, S. G. Gopalakrishnan, B. Key, W. D. Richards, S. Tan, Y. Tian, Y. Wang, J. Li, G. Ceder, *Nat. Commun.* **2017**, *8*, 1759.
- [32] L. P. Wang, Z. Zhao-Karger, F. Klein, J. Chable, T. Braun, A. R. Schür, C. R. Wang, Y. G. Guo, M. Fichtner, *ChemSusChem* **2019**, *12*, 2286.
- [33] Q. Zhang, H. Hao, H. Zhang, S. Wang, J. Jin, D. Sun, *Eur. J. Inorg. Chem.* **2013**, *7*, 1123.
- [34] J. L. Wang, K. L. Hou, F. Y. Bai, Y. H. Xing, Z. Shi, *Struct. Chem.* **2012**, *23*, 275.
- [35] D. E. Kravchenko, A. J. Cruz, S. Rodríguez-Hermida, N. Wauteraerts, T. Hauffman, R. Ameloot, *Chem. Mater.* **2020**, *32*, 10469.
- [36] A. Rossin, M. R. Chierotti, G. Giambastiani, R. Gobetto, M. Peruzzini, *CrystEngComm* **2012**, *14*, 4454.
- [37] I. Spanopoulos, I. Bratsos, C. Tampaxis, A. Kourtellaris, A. Tasiopoulos, G. Charalambopoulou, T. A. Steriotis, P. N. Trikalitis, *CrystEngComm* **2015**, *17*, 532.
- [38] P. G. Bruce, C. A. Vincent, *J. Electroanal. Chem.* **1987**, *225*, 1.
- [39] J. Yang, J. Li, W. Gong, F. Geng, *Proc. Natl. Acad. Sci. USA* **2021**, *118*.
- [40] K. M. Anilkumar, B. Jinisha, M. Manoj, S. Jayalekshmi, *Eur. Polym. J.* **2017**, *89*, 249.
- [41] R. N. Singru, A. B. Zade, W. B. Gurnule, *J. Chem.* **2009**, *7*, 1878.

Manuscript received: June 9, 2022  
Revised manuscript received: July 6, 2022  
Accepted manuscript online: July 8, 2022  
Version of record online: July 27, 2022